Catal Lett (2016) 146:2185–2192
DOI 10.1007/s10562-016-1844-0

ZnS@g-C_3N_4 Composite Photocatalysts: In Situ Synthesis and Enhanced Visible-Light Photocatalytic Activity

Bin Xue[1] · Hai-Yun Jiang[1] · Tao Sun[1] · Fang Mao[1]

Received: 6 July 2016 / Accepted: 6 August 2016 / Published online: 22 August 2016

Abstract ZnS@g-C_3N_4 composite photocatalysts were synthesized by an in situ thermal polycondensation process under an inert atmosphere. The physicochemical properties of the ZnS@g-C_3N_4 composite photocatalysts were characterized by X-ray diffraction (XRD), X-ray photoelectron spectroscopy (XPS), transmission electron microscopy (TEM), UV–vis diffuse reflectance spectroscopy (UV–vis DRS), and photoluminescence (PL) spectroscopy. The characterization results displayed fine ZnS nanoparticles adhered to the surface of g-C_3N_4 nanosheets, and the presence of ZnS nanoparticles caused the split and exfoliation of g-C_3N_4 nanosheets. The ZnS@g-C_3N_4 composite photocatalysts exhibited the apparent visible-light absorption and the weakened recombination of photogenerated electron/hole pairs. The evaluation on photocatalytic degradation of rhodamine B (RhB) indicated the ZnS@g-C_3N_4 composite photocatalysts possessed large adsorption capacity and superior visible-light induced activity. Based on the trapping experiments of active species, the photocatalysis mechanism of the ZnS@g-C_3N_4 composite photocatalysts was also discussed.

Graphical Abstract

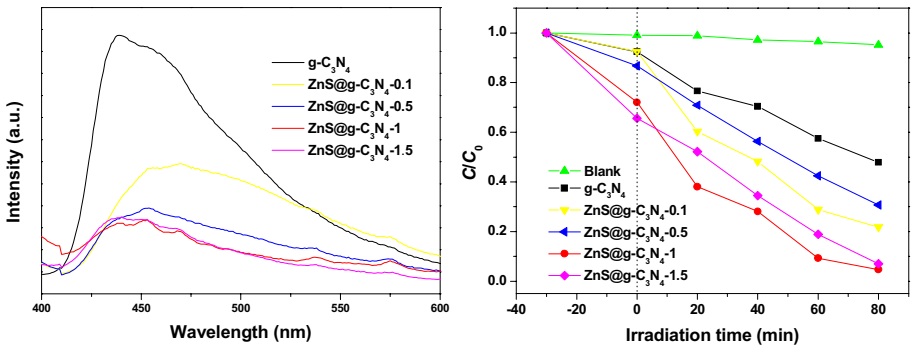

Keywords In situ synthesis · Photocatalysis · Organic pollutant degradation

1 Introduction

Along with the rapid development of human society, the environmental pollution and energy shortage are serious problems in today's world. A large amount of pollutants

Electronic supplementary material The online version of this article (doi:10.1007/s10562-016-1844-0) contains supplementary material, which is available to authorized users.

✉ Bin Xue
bxue@shou.edu.cn; binxue_chem@yahoo.com

[1] Department of Chemistry, College of Food Science and Technology, Shanghai Ocean University, Shanghai 201306, China

such as dyes, pesticides, heavy metals, antibiotics and so on severely threatens to human health and ecological security. Use of clean and sustainable energy to achieve environmental remediation represents the general trend [1–4]. Among a variety of environmental remediation technologies, photocatalytic degradation of pollutants is a promising technology because of environmental friendliness and energy conservation. In recent years, the exploration of high-efficiency photocatalysts has attracted more and more attention [5–9].

Graphitic carbon nitride (g-C_3N_4), a new polymeric semiconductor, can be used in photocatalytic degradation of pollutants, hydrogen production, oxygen evolution and CO_2 reduction because of its narrow bandgap, good stability, low-cost and environmental friendliness [10–18]. However, the photocatalytic activity of pristine g-C_3N_4 still needs to be improved under visible-light irradiation due to rapid recombination of photogenerated electron/hole pairs, low absorption and small specific surface area [10–14]. In order to overcome the above drawbacks, a series of strategies, for examples, exfoliation of into nanosheets [19–21], fabrication of hierarchical structures [22], construction of porous structures [23, 24], protonation [25], doping [26], defect engineering [27], fabrication of heterostructures [28–33], are applied to the design and synthesis of g-C_3N_4 based-photocatalysts. Among various modified approaches, the fabrication of heterostructures has been extensively studied due to a wide choice of heterogenous components (wide bandgap semiconductor, narrow bandgap semiconductors, precious metals and so on) and high separation efficiency of photogenerated electron/hole pairs. Compared to the usual multi-step synthesis, in situ synthesis of g-C_3N_4 based-heterostructures under thermal polycondensation conditions has obvious advantages, such as convenience, speediness and atom economy and so on. However, to the best of our knowledge, little work has been made to the in situ synthesis of metal sulphide@g-C_3N_4 composite photocatalysts. This may be attributed to difficult to control together growing of g-C_3N_4 and metal sulphide under calcination conditions.

In this paper, we reported an in situ synthesis of ZnS@g-C_3N_4 composite photocatalysts by a thermal polycondensation route under an inert atmosphere. In the in situ synthesis, we choose thiourea acts both as a precursor of g-C_3N_4 and a sulfur source of ZnS. This protocol achieves the effective incorporation between g-C_3N_4 and ZnS. The ZnS@g-C_3N_4 composite photocatalysts exhibit the superior visible-light responsive photocatalytic activity for degredation of rhodamine B (RhB).

2 Experimental

All chemicals were of analytical grade without further purification.

2.1 Fabrication of Precursor

In a typical precursor fabrication process, 1.0 g of $Zn(NO_3)_2{\cdot}6H_2O$ and 10 g of thiourea were dissolved in 50 mL of deionized water, and then evaporated and dried 12 h at 100 °C. Thus, white precursor was obtained.

2.2 Synthesis of ZnS@g-C_3N_4

In a typical synthesis, the white precursor in a porcelain boat with a cover was placed at the centre in a tube furnace, as a supplementary sulfur source, a quantity of thiourea in another porcelain boat was placed at the upstream of the gas flow, and then calcined at 550 °C for 2 h at a heat rate of 25 °C min^{-1} under a high purity nitrogen (≥99.999 %) atmosphere. Finally, yellow-white ZnS@g-C_3N_4 powders was obtained. Based on the feeding amount of $Zn(NO_3)_2{\cdot}6H_2O$, the as-synthesized ZnS@g-C_3N_4 photocatalysts were denoted as ZnS@g-C_3N_4-1. According to the above procedure, a series of ZnS@g-C_3N_4 composite photocatalysts were synthesized through changing dose of $Zn(NO_3)_2{\cdot}6H_2O$, and denoted as ZnS@g-C_3N_4-0.1, ZnS@g-C_3N_4-0.5 and ZnS@g-C_3N_4-1.5, respectively.

2.3 Characterizations

XRD patterns of the samples were recorded using a Bruker D8 ADVANCE diffractometer with monochromatized CuKα radiation (λ = 0.1540562 nm). The operating voltage and current were 40 kV and 40 mA, respectively. TEM was performed on Hitachi H-800 microscope under an acceleration voltage of 200 kV. The Brunauer-Emmett-Teller (BET) specific surface area was measured using a Micromeritics ASAP 2020 instrument. XPS was recorded using a Kratos Axis Ultra DLD spectrometer employing a monochromated Al-Kα X-ray source. In order to subtract the surface charging effect, the C1s peak has been fixed at a binding energy of 284.6 eV. UV–vis DRS of the samples were obtained on a UV–visible spectrophotometer (Hitachi U-3900). PL spectrum measurements were carried out with a luminescence spectrometer (Edinburgh Instruments FS5) using 370 nm as the excitation wavelength at room temperature.

2.4 Photocatalytic Activity Measurements

In a typical photocatalytic degradation measurement for RhB, 50 mg of photocatalysts was added to 100 mL of a 10 mg L^{-1} RhB solution and then stirred in the dark for 30 min to ensure adsorption equilibrium. The suspension was then exposed to visible-light irradiation from a 350 W Xe lamp with a filter (>420 nm) at a distance of 20 cm. After various reaction times, the photocatalysts were removed by centrifugation and the RhB solution concentrations were

analyzed by measuring the maximum absorbance at 554 nm using a UV–Vis spectrophotometer (HITACHI U-3900). In recycling experiments, after completion of aforementioned photodegradation, the solid photocatalysts were removed by centrifugation, washed several times with deionized water and vacuum dried 6 h at 80 °C. Then, the solid photocatalysts reused in the next cycle.

3 Results and Discussion

3.1 Photocatalyst Characterization

Figure 1 shows the XRD patterns of the samples. The strong diffraction peaks at 13.2° and 27.7° in the patterns of all samples correspond to the (100) and (002) planes of g-C_3N_4, respectively. Unlike the previously reported cases, a slight shift occurred in the position of peak for (002) plane from 27.4° to 27.7°. Similar phenomena have been reported [34]. The shift may be caused by the change of heating rate, precursors and additives under in situ synthesis conditions. The intensities of diffraction peaks of g-C_3N_4 gradually are reduced and the characteristic peaks of ZnS increasingly appear with the enhancement of loading amounts. The diffraction peaks of ZnS component correspond to the wurtzite phase of ZnS (JCPDS No. 39-1363). In addition, a trace amount of ZnO phase exists in the patterns of high loading samples. This may be attributed the partial pyrolysis of zinc nitrate precursor.

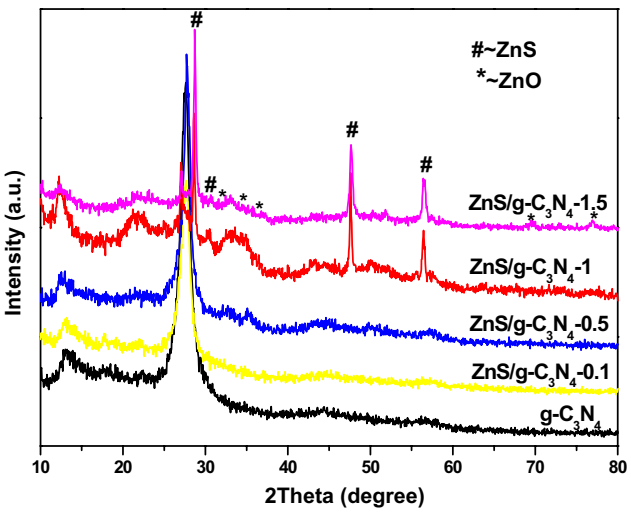

Fig. 1 XRD patterns of samples

Figure 2 displays the typical TEM images of pristine g-C_3N_4 and ZnS-modified g-C_3N_4 composite photocatalysts. As shown in Fig. 2a, the pristine g-C_3N_4 consists of curly nanosheets with a thickness of tens of nanometers. Figure 2b indicates ZnS nanoparticles in diameter of around 10–20 nm (as shown by arrow) are closely attached on the g-C_3N_4 nanosheets. The tight contact between ZnS nanoparticles and g-C_3N_4 nanosheets are beneficial to enhance photocatalytic activity of ZnS@g-C_3N_4 composite photocatalysts. In addition, ZnS@g-C_3N_4 composite photocatalysts possess crushing and thinner sheet-like structures compared with pristine g-C_3N_4, which may be attributed to the presence of ZnS nanoparticles changed the growth environment of g-C_3N_4. The more crushing and exfoliated structures could provide more adsorption sites for guest molecules.

XPS analysis reveals a surface chemical status of ZnS@g-C_3N_4 composite photocatalysts. Figure 3a shows the survey spectrum of ZnS@g-C_3N_4-1, indicated the existence of C, N, O, Zn and S elements. The signal of O 1s peak may be derived from absorption of H_2O, CO_2 and traces of ZnO. XPS spectrum of C 1s of ZnS@g-C_3N_4-1 is shown in Fig. 3b. The C 1s spectrum can be deconvoluted into three

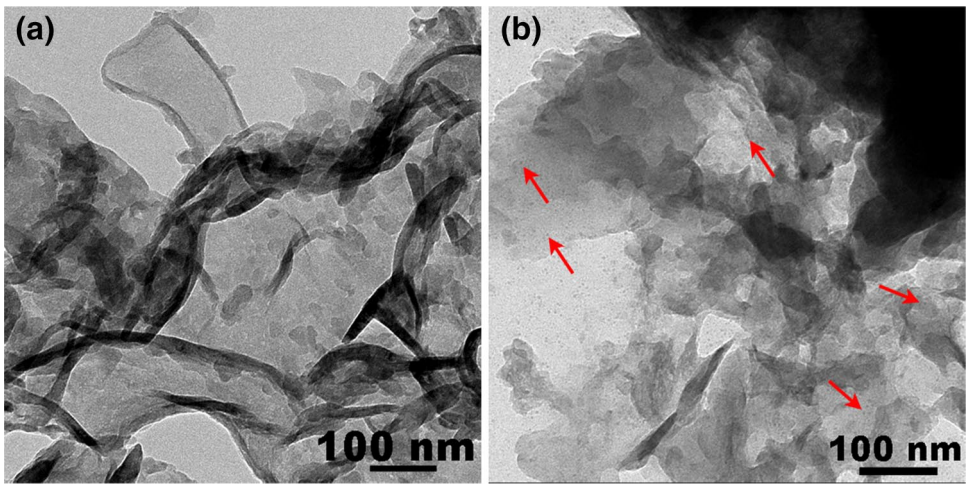

Fig. 2 TEM images of **a** pristine g-C_3N_4 and **b** ZnS@g-C_3N_4-1

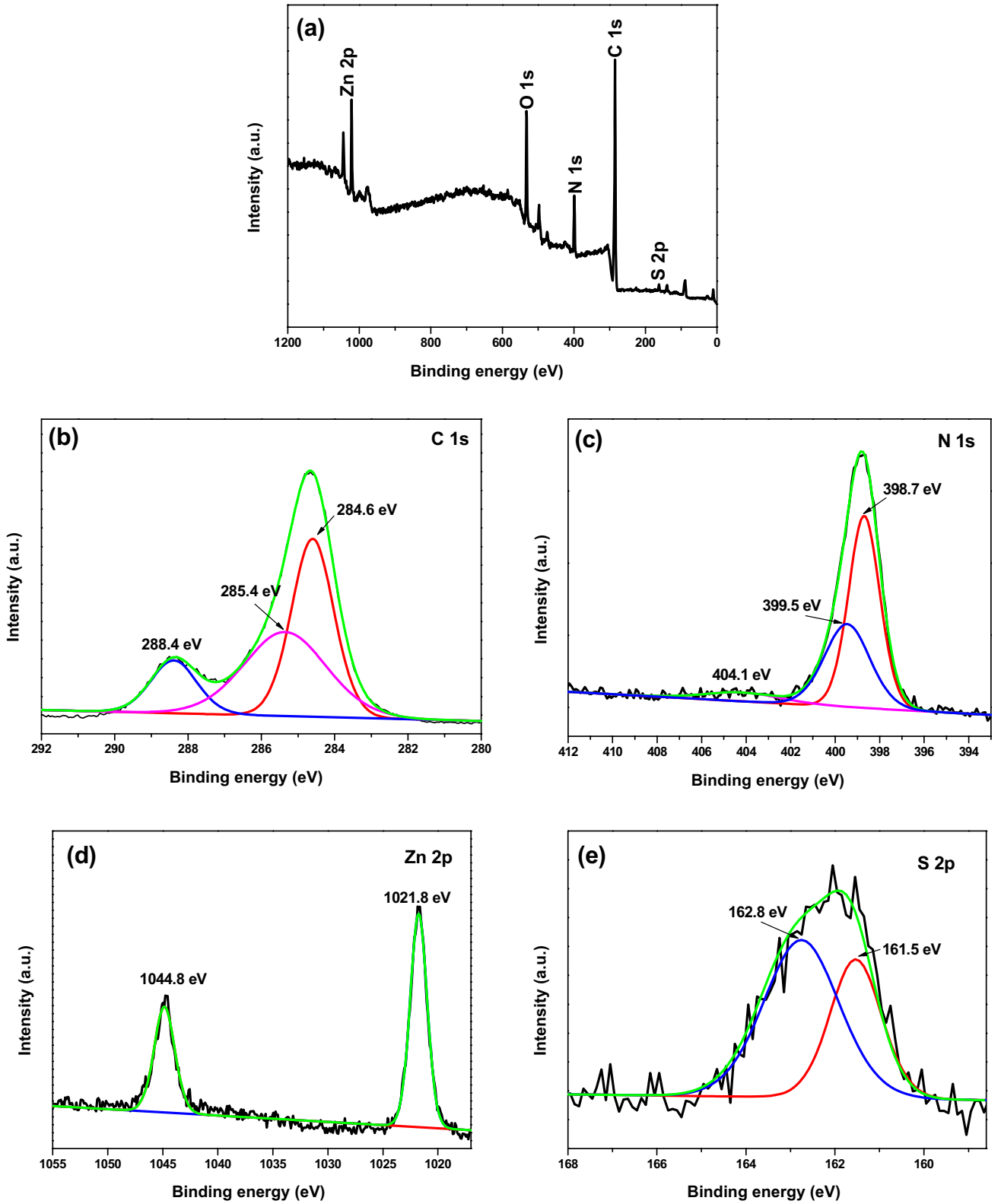

Fig. 3 XPS spectra of ZnS@g-C_3N_4-1: **a** survey spectrum, **b** C1s, **c** N 1 s, **d** Zn 2p and **e** S 2p

peaks at 284.6, 285.4 and 288.4 eV. The peak at 284.6 eV is attributed to sp^2 C–C bonds of graphitic sites in a CN network and hydrocarbon contamination from XPS instrument itself [35]. The peaks at 285.4 and 288.4 eV are assigned to sp^3 hybridized carbon (C–$(N)_3$) and sp^2-bonded carbon in N-containing aromatic rings (N–C=N), respectively [36].

Figure 3c displays three peaks appear at 398.7, 399.5 and 404.1 eV in deconvolution of the N 1s spectrum, which can be ascribed to sp^2-bonded N in the triazine rings (C–N = C), the tertiary nitrogen (N–$(C)_3$) groups and the charging effects or positive charge localization in the heterocycles, respectively [37]. As shown in Fig. 3d, the Zn 2*p* spectrum exhibits two characteristic peaks at 1021.8 and 1044.8 eV, which is corresponding to the binding energies of Zn $2p_{3/2}$ and Zn $2p_{1/2}$ states of Zn^{2+}, respectively [38]. As shown in Fig. 3e, two peaks appear at 161.5 and 162.8 eV in deconvolution of the S 2*p* spectrum can be ascribed to the binding energies of S $2p_{3/2}$ and S $2p_{1/2}$ of S^{2-}, respectively [39].

The optical properties of the samples were explored. Figure 4a shows the UV–vis DRS of the samples. The pristine g-C_3N_4 exhibits strong visible-light absorption bands, which can be assigned to the n–p* transitions involving lone pairs on the edge of the N atoms of the triazine/heptazine rings [18]. Unlike g-C_3N_4 prepared using dicyandiamide or melamine as raw materials [37], the absorption edge of the pristine g-C_3N_4 extended from 450 to 600 nm. This could be attributed to the enriched nitrogen modified the band structure of g-C_3N_4 [36]. After loading of ZnS component, ZnS@g-C_3N_4 composite photocatalysts exhibit strong UV-light absorption, which can be assigned to electronic transitions from the valence band (VB) to the conduction band (CB) of ZnS [40]. The bandgap energies (E_g) of the pristine g-C_3N_4 and ZnS@g-C_3N_4-1 can be calculated from the intercept of the tangents to the plots of $(\alpha h\nu)^{1/2}$ *vs.* $h\nu$, where α, h and ν are absorption coefficient, Planck's constant and light frequency, respectively [36, 41]. Therefore, as shown in Fig. S1, the E_g of the pristine g-C_3N_4 and ZnS@g-C_3N_4-1 were estimated to be 2.46 and 2.33 eV, respectively. Compared to the pristine g-C_3N_4, the E_g of ZnS@g-C_3N_4-1 has been reduced, which is consistent with the enhancement of visible-light absorption. The phenomenon may be related to the strong coupling between ZnS and g-C_3N_4 [42].

It is well known that the photocatalytic activity of photocatalysts is closely related with the recombination of photogenerated electron/hole pairs [16]. The PL spectroscopy is a powerful tool to probe the recombination of photogenerated electron/hole pairs [43]. As shown in Fig. 4b, the strong PL intensity of the pristine g-C_3N_4 indicates that the rapid recombination of photogenerated electron/hole pairs in photocatalytic process of g-C_3N_4. However, the waning PL intensities of ZnS@g-C_3N_4 composite photocatalysts suggest that the recombination of photogenerated electron/hole pairs is gradually weakened. This indicates the coupling of ZnS nanoparticles and g-C_3N_4 effectively suppressed the recombination of photogenerated electron/hole pairs. As a result, ZnS@g-C_3N_4-1 with optimal loadings displays strongest ability to inhibit the recombination of photogenerated electron/hole pairs. Obviously, the enhanced visible-light response and the weakened recombination of photogenerated electron/hole pairs may promote the photocatalytic activities of ZnS@g-C_3N_4 composite photocatalysts.

3.2 Photocatalytic Activity

The photocatalytic activity of ZnS@g-C_3N_4 composite photocatalysts was evaluated by photocatalytic degradation of RhB solution under visible-light irradiation. Figure 5a shows time curves of photocatalytic degradation of RhB for various samples. The adsorption behaviours of photocatalysts are explored before light irradiation. After stirring for 30 min in dark, primary g-C_3N_4 and ZnS@g-C_3N_4-0.1 display lower adsorption capacities (~7.5%). However, the adsorption capacities of ZnS@g-C_3N_4 composite photocatalysts are improved significantly with the increased load of ZnS. The adsorption capacity of ZnS@g-C_3N_4-1 reaches

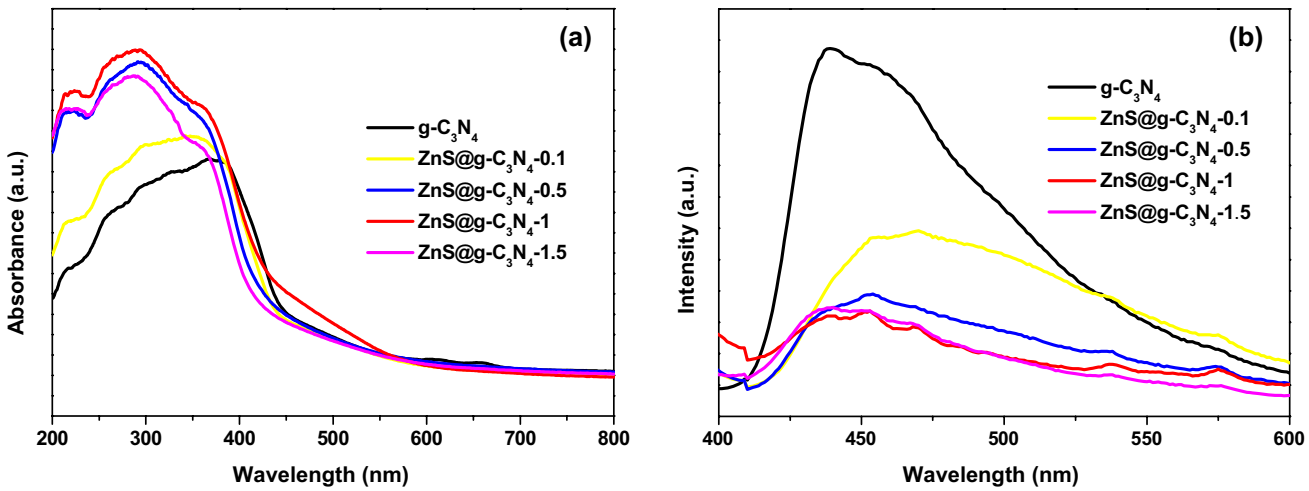

Fig. 4 **a** UV–vis DRS and **b** PL spectra of samples

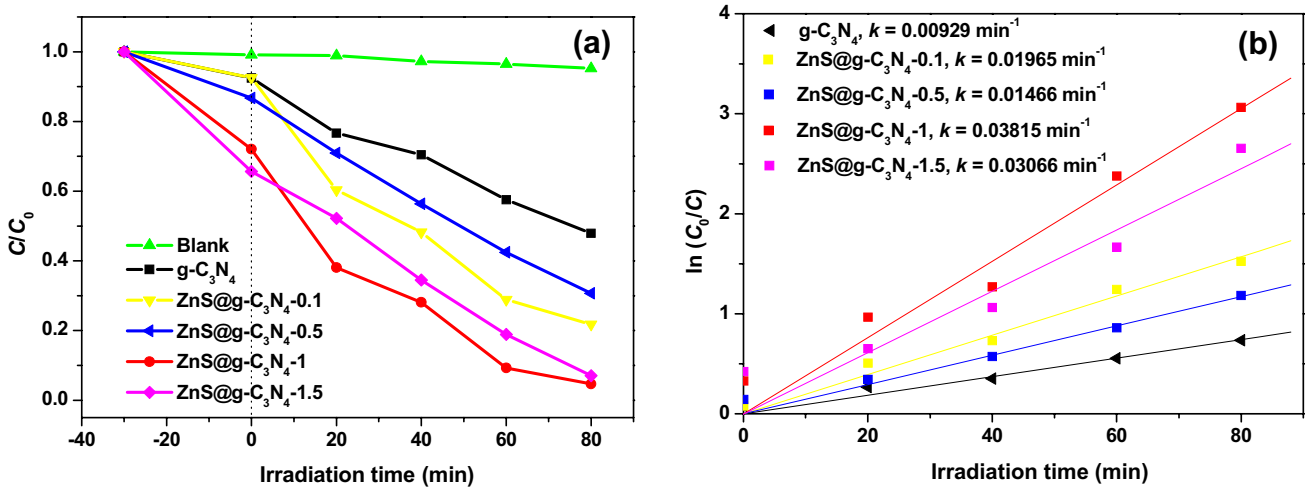

Fig. 5 **a** Photocatalytic activity of samples and **b** pseudo-first-order kinetic plots for the photocatalytic degradation of RhB

28.0%. The specific surface areas of primary g-C_3N_4 and ZnS@g-C_3N_4-1 were 76.0 and 63.1 $m^2\ g^{-1}$, respectively. The specific surface area of ZnS@g-C_3N_4 composite photocatalysts decreases due to the loading of ZnS nanoparticles, but ZnS@g-C_3N_4-1 still have a larger adsorption capacity, which suggested the crushing and exfoliated nanosheet structures could provide more active sites to adsorb RhB molecules [44]. The higher adsorption capacities of ZnS@g-C_3N_4 composite photocatalysts could promote photocatalytic activities. In a blank experiment, 4.8% of RhB has been degraded in the absence of any photocatalysts after visible-light irradiation of 80 min, which indicated self-photodegradation of RhB is negligible for the evolution of photocatalytic activities. Moreover, the degradation rate of RhB can reach 52.1% within 80 min in the presence of primary g-C_3N_4 under visible-light irradiation, which could be attributed to its stronger visible-light absorption properties [36, 37]. The photocatalytic activities of ZnS@g-C_3N_4 composite photocatalysts have been further improved. Among various composite photocatalysts, the ZnS@g-C_3N_4-1 composite photocatalysts reach hightest degradation rate (95.3%) within 80 min under visible-light irradiation.

In order to further quantitatively compare the photocatalytic activities of the various photocatalysts, the experimental data in Fig. 5a were analyzed by the pseudo-first-order model:

$$\ln\left(C_0 / C\right)=kt.$$

Here, k is the rate constant, t is reaction time, C_0 is the initial concentration of RhB and C is the concentration of RhB at reaction time t. Fig. 5b exhibits the kinetic analysis results. The photocatalytic activities of all the photocatalysts are in the following order: ZnS@g-C_3N_4-1 > ZnS@g-C_3N_4-1.5 > ZnS@g-C_3N_4-0.1 > ZnS@g-C_3N_4-0.5 > g-C_3N_4. The results indicated that the present of ZnS nanoparticles

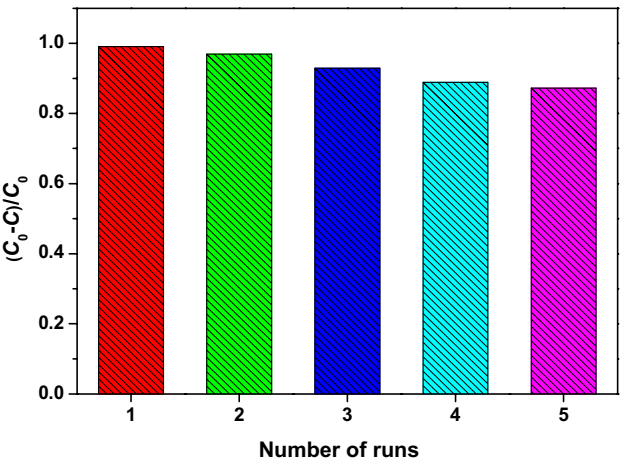

Fig. 6 Recycling stability of ZnS@g-C_3N_4-1

enhances distinctly the photocatalytic activity owing to improve the adsorption capacity and inhibit the recombination of photogenerated electron/hole pairs.

The recycling experiments of ZnS@g-C_3N_4-1 composite photocatalysts were performed in order to investigate the stability of ZnS@g-C_3N_4 composite photocatalysts. As shown in Fig. 6, the degradation rate of RhB remains at 87.2% after five runs of photocatalysis. Moreover, as shown in Fig. S2, XRD pattern of the ZnS@g-C_3N_4-1 composite photocatalysts recovered after the fifth cycle did not change significantly compared to the fresh sample. The recycling experiments show that ZnS@g-C_3N_4 composite photocatalysts would be suitable for repeated applications.

3.3 Photocatalysis Mechanism

In order to probe into the photocatalysis mechanism of ZnS@g-C_3N_4 composite photocatalysts during

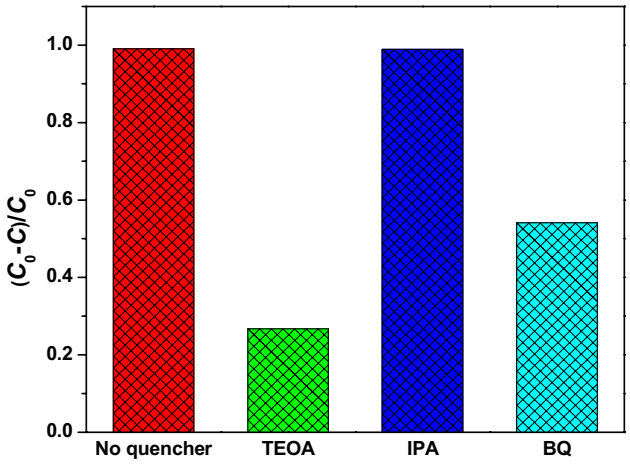

Fig. 7 Radical trapping experiment results

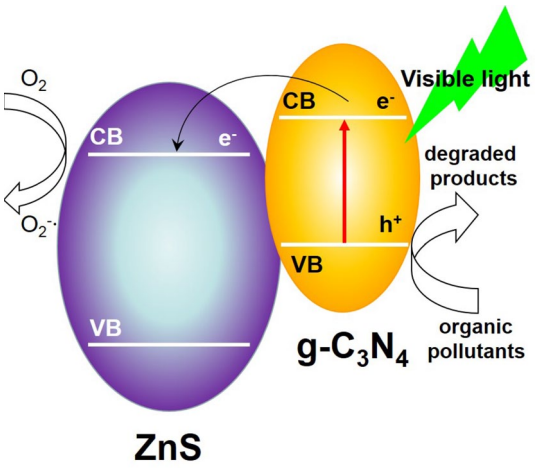

Fig. 8 Schematic diagram of photocatalysis over ZnS@g-C_3N_4 composite photocatalysts

photodegradation of RhB under visible-light irradiation, a series of radical trapping experiment were performed. The results are shown in Fig. 7. When TEOA (1 mmol L^{-1}, a quencher of hole) or BQ (1 mmol L^{-1}, a quencher of $O_2^{\cdot-}$) introduce into photocatalytic reaction system prior to addition of the ZnS@g-C_3N_4-1 composite photocatalysts, the photodegradations of RhB are significantly inhibited. Conversely, the degradation of RhB is hardly affected by the addition of IPA (1 mmol L^{-1}, a quencher of ·OH). Obviously, hole and $O_2^{\cdot-}$ are the dominated reactive species during photodegradation of RhB by the ZnS@g-C_3N_4-1 composite photocatalysts under visible-light irradiation.

Based on the radical trapping experimental results, a possible photocatalysis mechanism over ZnS@g-C_3N_4 composite photocatalysts was proposed in Fig. 8. Type II heterojuction at the interface between ZnS and g-C_3N_4 can build up due to appropriate band alignment [45]. Under visible-light irradiation, g-C_3N_4 can be excited to form photogenerated electron/hole pairs owing to narrow bandgap energy [29]. However, ZnS has no visible-light response owing to its wide bandgap [46]. Due to the more positive CB position of ZnS [46] with respect to the CB position of g-C_3N_4 [29], the photogenerated electrons can be transferred from the CB of g-C_3N_4 to the CB of ZnS. Further, the photogenerated electrons can react with O_2 to produce $O_2^{\cdot-}$. Meanwhile, owing to the more negative VB position of g-C_3N_4 [46] with respect to the VB of ZnS [29], the photogenerated holes are unable to migrate from the VB of g-C_3N_4 to the VB of ZnS and remain in the VB of g-C_3N_4. Finally, $O_2^{\cdot-}$ and hole as the reactive species degrade organic pollutants by oxidation. As a result, the matched CB edge potential and tightly coupling of ZnS and g-C_3N_4 in ZnS@g-C_3N_4 composite photocatalysts efficiently improve the separation of photogenerated electron/hole pairs and enhances photocatalytic activity.

4 Conclusions

We have successfully synthesized ZnS@g-C_3N_4 composite photocatalysts by an in situ thermal polycondensation route. It is found that the monodispersed ZnS nanoparticles in the diameter of tens of nanometers uniformly were distributed on the surfaces of crushing and exfoliated g-C_3N_4 nanosheets. The existence of ZnS nanoparticles obviously suppressed the recombination of photogenerated electron/hole pairs in the ZnS@g-C_3N_4 composite photocatalysts. Compared to pristine g-C_3N_4, the ZnS@g-C_3N_4 composite photocatalysts exhibited superior visible-light responsive photocatalytic activity for RhB degradation. The enhancement in photocatalytic activity of ZnS@g-C_3N_4 composite photocatalysts can be ascribed to large adsorption capacity and high separation efficiency of photogenerated electron/hole pairs in the heterojunction interface between ZnS nanoparticles and g-C_3N_4 nanosheets. This work provided a facile and universal route for the synthesis of metal sulphide@g-C_3N_4 composite photocatalysts, which will promote the practical application of g-C_3N_4-based composite photocatalysts.

Acknowledgments This work was financially supported by Shanghai Ocean University (Project: A2-0203-00-100529).

References

1. Nocera DG (2009) Chem Soc Rev 38:13
2. Zhang HJ, Chen GH, Bahnemann DW (2009) J Mater Chem 19:5089
3. Sovacool BK (2012) Energy Environ Sci 5:9157
4. Shen YF (2015) J Mater Chem A 3:13114
5. Li X, Yu JG, Jaroniec M (2016) Chem Soc Rev 45:2603
6. Ansari SA, Khan MM, Ansaric MO, Cho MH (2016) New J Chem 40:3000

7. Li Y, Xu H, Ouyang SX, Ye JH (2016) Phys Chem Chem Phys 18:7563
8. Ueno K, Oshikiri T, Misawa H (2016) ChemPhysChem 17:199
9. An CH, Wang ST, Sun YG, Zhang QH, Zhang J, Wang CY, Fang JY (2016) J Mater Chem A 4:4336
10. Dong GP, Zhang YH, Pan QW, Qiu JR (2014) J Photochem Photobio C 20:33
11. Cao SW, Yu JG (2014) J Phys Chem Lett 5:2101
12. Yin SM, Han JY, Zhou TH, Xu R (2015) Catal Sci Technol 5:5048
13. Patnaik S, Martha S, Acharya S, Parida KM (2016) Inorg Chem Front 3:336
14. Patnaik S, Martha S, Parida KM (2016) RSC Adv 6:46929
15. Martha S, Nashim A, Parida KM (2013) J Mater Chem A 1:7816
16. Samanta S, Martha S, Parida K (2014) ChemCatChem 6:1453
17. Panyab S, Parida KM (2015) Phys Chem Chem Phys 17:8070
18. Nayak S, Mohapatra L, Parida K (2015) J Mater Chem A 3:18622
19. Dong XP, Cheng FX (2015) J Mater Chem A 3:23642
20. Tong JC, Zhang L, Li F, Li MM, Cao SK (2015) Phys Chem Chem Phys 17:23532
21. Bu YY, Chen ZW, Xie T, Li WB, Ao JP (2016) RSC Adv 6:47813
22. Huang ZJ, Li FB, Chen BF, Yuan GQ (2016) ChemSusChem 9:478
23. Wang YY, Ibad MF, Kosslick H, Harloff J, Beweries T, Radnik J, Schulz A, Tschierlei S, Lochbrunner S, Guo XY (2015) Microporous Mesoporous Mater 211:182
24. Zhang YW, Liu JH, Wu G, Chen W (2012) Nanoscale 4:5300
25. Wei HT, Zhang Q, Zhang YC, Yang ZJ, Zhu AP, Dionysiou DD (2016) Appl Catal A 521:9
26. Hong JD, Xia XY, Wang YS, Xu R (2012) J Mater Chem 22:15006
27. Tay QL, Kanhere P, Ng CF, Chen S, Chakraborty S, Huan ACH, Sum TC, Ahuja R, Chen Z (2015) Chem Mater 27:4930
28. Liao GZ, Chen S, Quan X, Yu HT, Zhao HM (2012) J Mater Chem 22:2721
29. Dong F, Zhao ZW, Xiong T, Ni ZL, Zhang WD, Sun YJ, Ho WK (2013) ACS Appl Mater Interfaces 5:11392
30. Huang LY, Xu H, Li YP, Li HM, Cheng XN, Xia JX, Xu YG, Cai GB (2013) Dalton Trans 42:8606
31. Chen J, Shen SH, Guo PH, Wang M, Wu P, Wang XX, Guo LJ (2014) Appl Catal B 152–153:335
32. Wang J, Guo P, Guo QS, Jönssona PG, Zhao Z (2014) CrystEngComm 16:4485
33. Li JH, Liu YL, Li HM, Chen C (2016) J Photochem Photobio A 317:151
34. Shan WJ, Hu Y, Bai ZG, Zheng MM, Wei CH (2016) Appl Catal B 188:1
35. Ge L, Han CC, Liu J, Li YF (2011) Appl Catal A 409:215
36. Dong F, Sun YJ, Wu LW, Fu M, Wu ZB (2012) Catal Sci Technol 2:1332
37. Zhang GG, Zhang JS, Zhang MW, Wang XC (2012) J Mater Chem 22:8083
38. Lv HL, Ji GB, Yang ZH, Liu YS, Zhang XM, Liu W, Zhang HQ (2015) J Colloid Inter Sci 450:381
39. Jia FZ, Yao ZP, Jiang ZH (2012) Int J Hydrog Energy 37:3048
40. Yue S, Wei BW, Guo XD, Yang SX, Wang LY, He J (2016) Catal Comm 76:37
41. Zheng Y, Jiao Yan, Zhu YH, Li LH, Han Y, Chen Y, Du AJ, Jaroniec M, Qiao SZ (2014) Nature Comm 5:3783
42. Li KX, Zeng ZX, Yan LS, Huo MX, Guo YH, Luo SL, Luo XB (2016) Appl Catal B 187:269
43. Li JX, Dai WL, Wu GJ, Guan NJ, Li LD (2015) Catal Commun 65:24
44. Shi L, Liang L, Wang FX, Liu MS, Liang T, Chen KL, Sun JMRSCA (2015) 5:63264
45. Moniz SJA, Shevlin SA, Martin DJ, Guo ZX, Tang JW (2015) Energy Environ Sci 8:731
46. Wang XW, Li YN, Wang MR, Li WJ, Chen MF, Zhao Y (2014) New J Chem 38:4182